J. Fluid Mech., (2012), *vol.* 708, *pp.* 469–479.

doi:10.1017/jfm.2012.319

Micro-bubble morphologies following drop impacts onto a pool surface

S. T. Thoroddsen[1]†, M.-J. Thoraval[1], K. Takehara[2] and T. G. Etoh[2]

[1] Division of Physical Sciences and Engineering and Clean Combustion Research Center, King Abdullah University of Science and Technology (KAUST), Thuwal 23955-6900, Saudi Arabia

[2] Department of Civil and Environmental Engineering, Kinki University, Higashi-Osaka 577-8502, Japan

(Received 16 April 2012; revised 15 June 2012; accepted 21 June 2012;
first published online 14 August 2012)

When a drop impacts at low velocity onto a pool surface, a hemispheric air layer cushions and can delay direct contact. Herein we use ultra-high-speed video to study the rupture of this layer, to explain the resulting variety of observed distribution of bubbles. The size and distribution of micro-bubbles is determined by the number and location of the primary punctures. Isolated holes lead to the formation of bubble necklaces when the edges of two growing holes meet, whereas bubble nets are produced by regular shedding of micro-bubbles from a sawtooth edge instability. For the most viscous liquids the air film contracts more rapidly than the capillary–viscous velocity through repeated spontaneous ruptures of the edge. From the speed of hole opening and the total volume of micro-bubbles we conclude that the air sheet ruptures when its thickness approaches ∼100 nm.

Key words: breakup/coalescence, drops, thin films

1. Introduction

The impact of a drop onto a pool surface can greatly enhance the gas transfer through the liquid–air interface and is therefore of interest in diverse fields such as climate and marine science, e.g. Wanninkhof *et al.* (2009) and Czerski *et al.* (2011). The bursting of a submicron gas film is also important to understanding the fundamental mechanisms involved in film breakup (Reiter & Sharma 2001; Neitzel & Dell'Aversana 2002; de Gennes, Brochard-Wyart & Quéré 2004; Reyssat & Quéré 2006) and the micro-bubbles generated can enhance nucleate boiling (Dhir 1998). For low impact velocities, the air under the drop cushions the impact and prevents immediate contact. This layer can stretch into a submicron hemispheric film of air, which either causes rebounding of the drop (Couder *et al.* 2005) or ruptures to form a myriad of entrapped micro-bubbles. The details of this rupture are unknown, principally due to the very rapid capillary-driven motions. Mesler and co-workers (Esmailizadeh & Mesler 1986; Sigler & Mesler 1990) presented a series of papers showing snapshots of bubble structures for water, without time-resolved imaging.

† Email address for correspondence: sigurdur.thoroddsen@kaust.edu.sa

Liquid	Density ρ (g cm^{-3})	Viscosity μ (cP)	Surf. tens. σ (dyn cm^{-1})	Cap. length a (mm)	Capill. velo. σ/μ (m s^{-1})	Crit. thick. δ_* $2\mu^2/(\rho\sigma)$ (μm)
Distilled water	0.997	0.894	72.1	2.72	80.6	0.0222
Perfluorohexane	1.710	1.1	11.9	0.842	10.8	0.120
Silicone oil 0.65	0.760	0.494	15.9	1.46	32.2	0.0404
Silicone oil 1	0.818	0.818	16.9	1.45	20.7	0.0968
Silicone oil 5	0.915	4.57	19.7	1.48	4.31	2.32
Silicone oil 10	0.935	9.35	20.1	1.48	2.15	9.30
Silicone oil 30	0.955	28.6	20.8	1.49	0.726	82.6
Silicone oil 100	0.965	96.5	20.9	1.49	0.217	923
Silicone oil 350	0.970	340	21.1	1.49	0.0622	11 300
Silicone oil 1000	0.970	970	21.2	1.49	0.0219	91 500

TABLE 1. Properties of the different liquids used in the experiments. Properties for Silicone oils are taken from the *ShinEtsu* data sheets.

Thoroddsen, Etoh & Takehara (2003) imaged detailed dynamics of the entrapment of a central bubble, along with a handful of realizations for film breakup for water drops. However, Mills, Saylor & Testik (2012) showed convincingly that the water case suffers from highly random film ruptures and is not repeatable, even if surfactants are included. Recently, Saylor & Bounds (2012) have shown that air film formation and breakup are much more repeatable for silicone oils than for water. We exploit this discovery to allow for precisely triggered observations with ultra-high-speed video imaging, at frame rates up to 1 million f.p.s. (Etoh *et al.* 2003), to explain the mechanisms underlying the variety of observed bubble morphologies, such as bubble necklaces and bubble nets.

2. Experimental setup

We use drops of silicone oils over a wide range of viscosities from $\nu = 0.65$ to 1000 cSt, as well as perfluorohexane liquid (C_6F_{14}), with properties given in table 1. The impact conditions are characterized by a Reynolds number $Re = \rho DU/\mu$ and a Weber number $We = \rho DU^2/\sigma$, where D is the drop diameter (1.6–3 mm) and U is the impact velocity ($\sim$0.5 m s^{-1}); ρ, μ and σ are respectively the density, dynamic viscosity and surface tension of the liquid. The ultra-high-speed video camera (Etoh *et al.* 2003) takes 102 frames with 312×260 px, irrespective of the frame rate used. In combination with a long-distance microscope we get down to a resolution of 2.1 μm px^{-1}.

3. Results

3.1. *Bubble morphology: hanging necklaces and bubble chandeliers*

Figure 1(*a*) shows a typical rupture of the highly stretched air film. Here the rupture occurs simultaneously at two points with the holes rapidly growing in size and travelling around the periphery leaving a *necklace* of bubbles where the holes meet, in a vertical plane. If only two holes are formed this is the inevitable resulting bubble structure, no matter how far apart these two holes are situated along the periphery, as there is always a vertical plane of symmetry cutting between these two holes. The gradual variation of bubble sizes along the necklace suggests that the

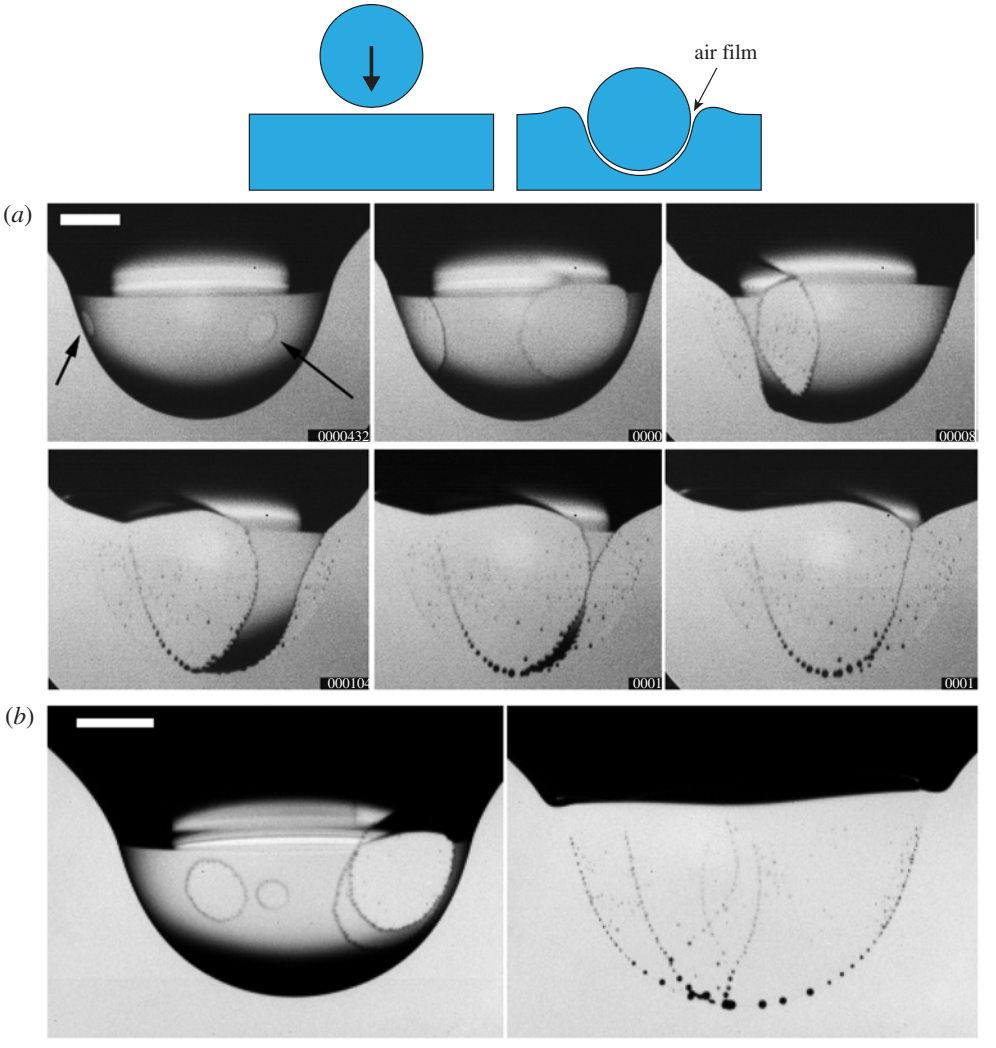

FIGURE 1. (Colour online) Typical formation of a hanging bubble necklace for silicone oil, $\nu = 10$ cSt, for $Re = 103$, $We = 21$, $D = 2.4$ mm, $U = 0.43$ m s^{-1}. (*a*) The air sheet punctures at two places (arrows), the right puncture is on the rear side of the axisymmetric air hemisphere. The frames are shown at 48, 208, 464, 656, 752 and 816 μs, relative to the time when the first rupture is observed. (*b*) Bubble lines following the rupture of six holes (four visible in the first frame, with two forming later on) as shown by the six final bubble lines. Frames shown at $t = 192$ and 800 μs after start of first rupture. Scale bars 500 μm. See also supplementary videos available at journals.cambridge.org/flm.

film thickness and its area are imprinted onto the necklace, i.e. where the film is thicker, the bubbles are larger and vice versa. This assumes the air flow within the thin film is insignificant compared to the motion of the edge. Based on the bubble size distribution, in figure 1(*a*), we infer that the film is thicker along the bottom and ruptures first at a fixed intermediate depth along the sidewall, where we expect the film to be thinnest, i.e. where the bubbles are smallest along the necklace and the film area is largest. Figure 1(*b*) shows another realization with six holes, which leaves six

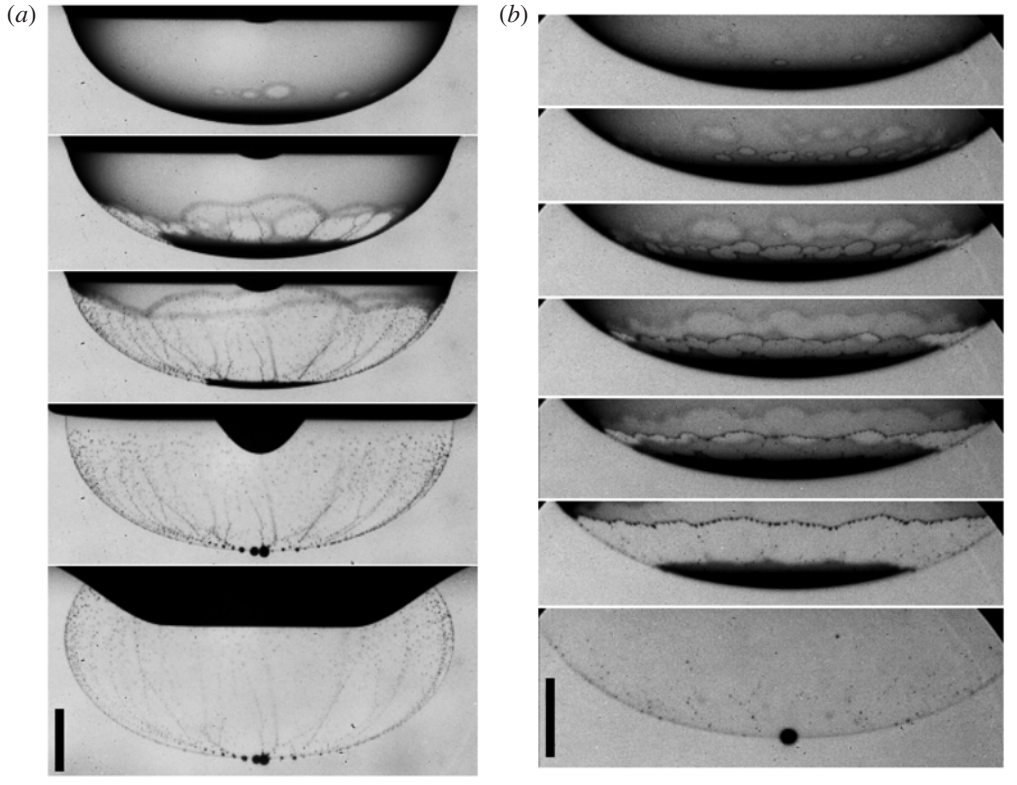

FIGURE 2. Typical bottom ring of ruptures leading to the formation of *bubble chandeliers* for $D = 2.4$ mm and (*a*) 5 cSt silicone oil, at $Re = 220$, $We = 24$, $U = 0.46$ m s^{-1}, shown at $t = 0$, 64, 160, 512 and 2656 μs after first puncture. (*b*) for 30 cSt silicone oil, at $Re = 50$, $We = 43$, $U = 0.63$ m s^{-1}. The first five frames are spaced by 32 μs. The bottom bubble has $d_b = 114$ μm, giving an average thickness of the bottom air-cap, below the ring of ruptures, as $\delta \simeq 250$ nm. The bars are 500 μm.

separate branches of bubbles. The net of bubble-lines is therefore a consequence of the original number and location of ruptures.

In figure 1 the isolated punctures in the air film appear when the impact is near the bouncing boundary where surface tension and viscous stresses have fully decelerated the drop, whereas for higher impact velocities the ruptures occur during stretching and thinning of the film. Ruptures therefore tend to occur at numerous locations simultaneously. Figure 2 shows such cases, where a multitude of ruptures occur along an azimuthal ring. This splits the hemisphere into two sections: one is pulled downwards to form a bottom bubble, whereas the rest is pulled upwards leaving faint vertical trails of micro-bubbles where the original holes meet. The edge moves much more rapidly up away from the ruptures, again suggesting a significantly thinner air layer along the sides. Similar formation of multiple holes along a ring may explain the *bubble chandeliers* observed in water (Sigler & Mesler 1990; Liow & Cole 2007; Mills *et al.* 2012).

Figure 3(*a*) shows the parameter regions, in terms of *We* and Ohnesorge ($Oh = \mu/\sqrt{\rho\sigma D}$) numbers, where the various breakup mechanisms occur. It identifies the lower boundary between bouncing drops and film rupture. This occurs at $We = 12$

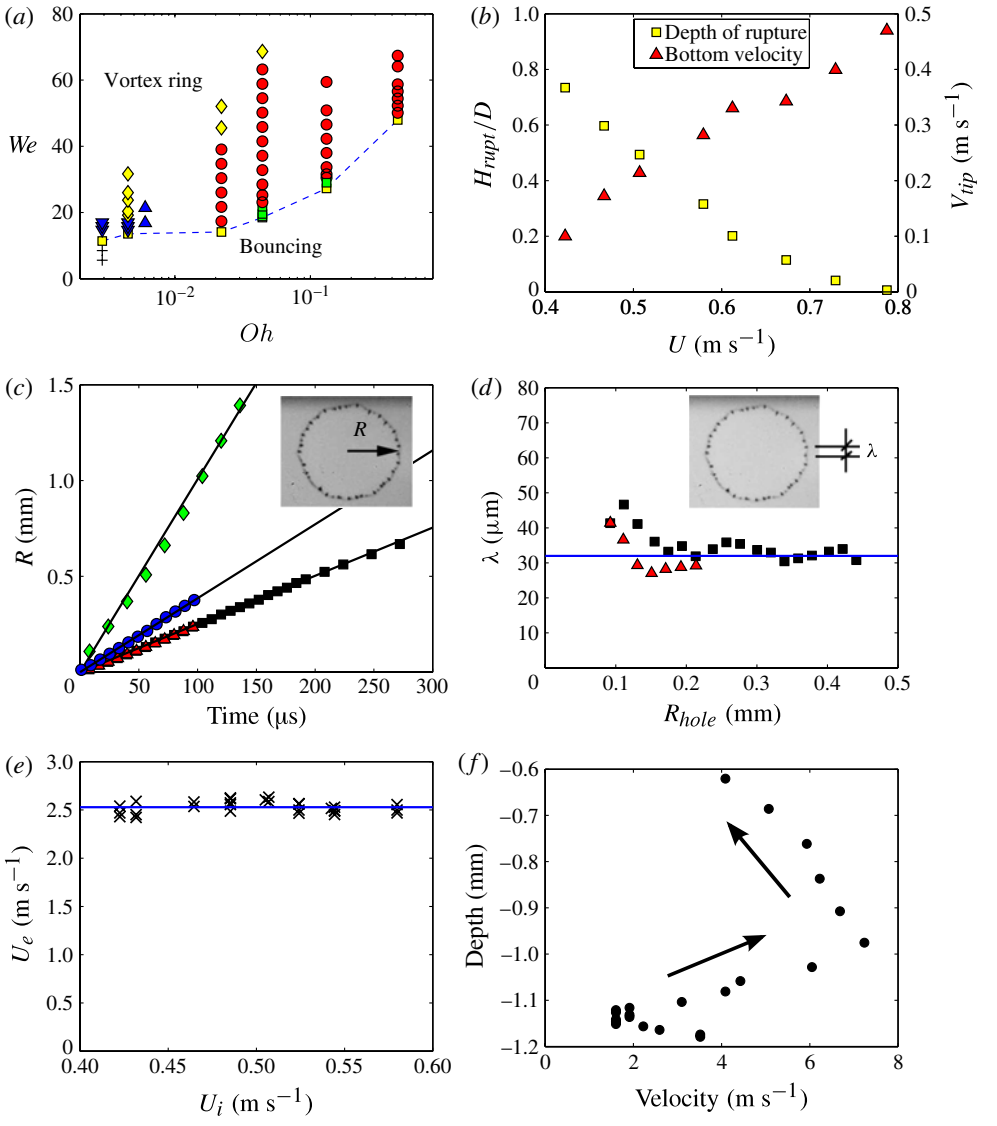

FIGURE 3. (*a*) Parameter space of the experiments for a range of silicone oil viscosities and impact velocities: □ upper boundary for bouncing drops; ■ isolated holes (<10 ruptures); ● multiple ruptures along an azimuthal ring; ▼and ▲central jet and bottom puncture, including experiments with perfluorohexane identified by ▲, ◆, early entrapment of a central air disk; +, film ruptures during late stage of crater rebound. (*b*) Depth of the ring of ruptures (□) and penetration velocity (▲) at the bottom tip of the air film at time of rupture, versus impact velocity, for 10 cSt and $Oh = 0.044$. (*c*) Horizontal hole radius versus time for silicon oils of 0.65 (◆), 5 (●) and 10 cSt (■, ▲). The holes open up at a nearly constant velocity of 11, 3.8 and 2.5 m s^{-1} respectively. (*d*) The average wavelength of the edge undulations for 10 cSt. (*e*) Horizontal rupture speed of the edge of the air film within 10 cSt silicon oil, measured for a range of different drop impact velocities, at $Oh = 0.044$. (*f*) The rupture velocity following the bottom tip rupture from a central jet. For perfluorohexane drop, corresponding to figure 5(*a*), $Re = 640$ and $We = 15$.

and 18 for 0.65 and 10 cSt silicone oils respectively, in good agreement with earlier results by Saylor & Bounds (2012). Figure 3(*b*) shows how the depth of the ring of ruptures moves progressively closer to the original free surface, as the drop impact velocity increases. This approaches the early entrapment of an air disk as studied by Thoroddsen *et al.* (2003).

We expect the punctures to occur by van der Waals forces destabilizing the very thin films ($\simeq$200 nm, Couder *et al.* 2005). The azimuthal spacing of the initial holes is $\sim$200 μm (estimated from second panel in figure 2*b*) which is in qualitative agreement with the wavelength λ which balances van der Waals and capillary pressures (Dorbolo *et al.* 2005), i.e. $\lambda = \delta^2/\sqrt{A/(6\pi\sigma)} \sim 100$ μm, where $\delta \simeq 200$ nm is the air film thickness, if we use 5×10^{-20} J for the Hamaker constant A, following Israelachvili (2011). The strong dependence on δ is in good agreement with new holes opening in time (figure 2), and the sharp transition from isolated holes to multiple ruptures as impact velocity increases, thinning the film more rapidly.

3.2. *Film thickness and speed of rupture*

During drop impacts the lubrication pressure in the air creates a dimple below the drop, thereby entrapping a bottom disk of air, as shown by Thoroddsen *et al.* (2003). Similar film thickness distributions are observed in numerous drainage films, as reviewed by Chan, Klaseboer & Manica (2011), and more recently by high-speed observations by van der Veen *et al.* (2012) for a water drop impacting a solid surface. The thinner air film along the side of the crater is also consistent with our observations of the film breaking on the side, and the final bubble distribution.

After rupture of the air film, it retracts under the action of surface tension. When viscous effects can be neglected, the velocity of the edge can be estimated by the Taylor–Culick velocity $u_\sigma = \sqrt{2\sigma/(\rho\delta)}$: see Oguz & Prosperetti (1989), Brenner & Gueyffier (1999), Song & Tryggvason (1999), Lhuissier & Villermaux (2011) and Gordillo *et al.* (2011). This approximation is valid for films thicker than $\delta_\star = 2\mu^2/(\rho\sigma)$. For our lowest viscosity case ($\nu = 0.65$ cSt), the edge velocity of 11 m s^{-1} (figure 3*c*) would correspond to $\delta = 350$ nm, consistent with previous estimates and much larger than $\delta_\star = 40$ nm (see table 1). However, for more viscous drops ($\nu = 5$ and 10 cSt), the edge velocity decreases, suggesting that viscous effects become important. Indeed, an estimate based on micro-bubble volumes gives a thickness on the side of $\delta \simeq 125$ nm, for $\nu = 10$ cSt in figure 4(*a*), smaller than $\delta_\star \sim 10$ μm. In this viscous-dominated regime, the edge velocity now scales as the capillary–viscous velocity $u_\mu = \sigma/\mu$: see Reyssat & Quéré (2006) and Aryafar & Kavehpour (2008). Note that δ no longer enters this relationship, as the driving surface tension and resisting viscous stress have the same dependence on the characteristic length scale δ. This is consistent with the edge velocity for 10 cSt in figure 3(*c*) where $Ca_e = u_e\mu/\sigma = 1.16$, i.e. viscous balanced. This transition is made clear in figure 6(*c*) by comparing experimental measurements with theory over a large range of viscosities.

3.3. *Rupture speed is independent of drop impact velocity*

As a consequence of the proposed van der Waals rupture mechanism, the local thickness of the film when it ruptures should be the same, irrespective of how the dynamics reached this air film thickness. Moreover, for this intermediate viscosity of 10 cSt, the edge velocity of such thin films is mostly influenced by viscosity and will not depend strongly on the film thickness. Therefore, we expect that the horizontal hole-opening rupture velocity will not depend on the drop impact velocity. We have verified this over a range of drop impact velocities where individual hole openings can

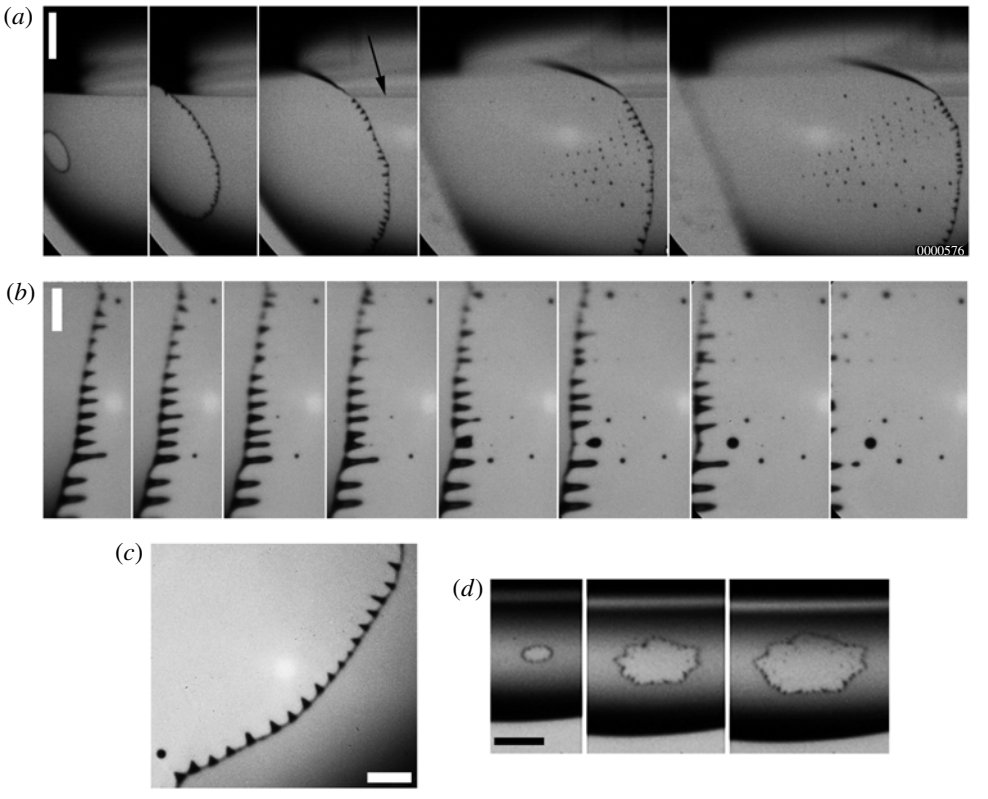

FIGURE 4. Typical formation of edge instabilities, for 10 cSt silicone oil in (*a,b,c*) and 100 cSt in (*d*). (*a*) Typical formation of a bubble net, at $Re = 100$, $We = 20$. The frames are shown 34, 130, 242, 418 and 514 μs after rupture. The bar is 200 μm. The average thickness of the air sheet can be estimated by assuming steady state in the air flow and measuring the area and bubble volume within the net at the vertical location of the rupture, giving $\delta \simeq 125$ nm $\pm$ 25 %. (*b,c*) Typical instability at the edge of the growing hole, for $Re = 127$, $We = 28$. The frames are spaced by 16 μs. Some teeth shed evenly spaced bubbles in a row, while a larger bubble is shed when two adjacent teeth merge. Micro-bubble diameters are here between 5 and 30 μm. The bar is 100 μm. (*c*) Regular meta-stable shark-tooth undulations, with the edge moving to the bottom right. The bar is 100 μm. (*d*) Star-like subharmonic undulations on the edge, for $Re = 19$, $We = 67$. The bar is 200 μm.

be measured, showing no significant variation in figure 3(*e*). These experiments were performed for a fixed Ohnesorge number $Oh = \mu/(\sqrt{\rho\sigma D}) = 0.044$, while varying the impact velocity.

3.4. *Edge instability: breakup of the growing edge*

The edge of the hole in the air layer does not initially shed bubbles, but grows thicker as it collects the air from the receding air layer and develops a spanwise instability leading to the separation of micro-bubbles. Figure 4 shows typical shapes of the expanding edge, revealing regular *teeth*, here spaced by ~38 μm. For new holes the undulations are already visible 34 μs after puncture, growing in amplitude, and the first micro-bubbles are shed 250 μs after the hole opens. For small holes, the

wavelength of the teeth is approximately constant, with new teeth growing or suddenly appearing between the old ones, as the length of the hole periphery grows (figure 3*d*). Closer to the bottom cap, the teeth become larger as the film is thicker. Two main mechanisms produce the bubbles, i.e. regular shedding from the tips of the teeth and secondly by the sideways motion of two adjacent teeth. When they merge they grow in size and pinch off a larger bubble. Both mechanisms are present in figure 4(*b*). The spacing of trailing bubbles is fairly regular, but they emerge at distinct locations along the front, often leaving behind a *bubble net*.

Figure 4(*c*) is a close-up of the teeth, which are initially stable. Their base and amplitude are about equal size, around 25 μm. They are therefore much wider than the thickness of the air sheet feeding them, and are thereby semi-stable and flat structures, consistent with numerical work of a retracting liquid edge (Bagué, Zaleski & Josserand 2007). The undulations end abruptly where the film becomes thicker, as the drop and free surface start to diverge from each other: see the arrow in the third frame in figure 4(*a*). The spacing of these teeth along the edge appears to be related to the local thickness of the air film. For example, in figure 4(*b*) they are wider when closer to the bottom of the curved interface.

3.5. *Bottom puncturing by a liquid jet*

The largest deformations of a drop, as it hits the pool surface, are expected for drops larger than the capillary length $a = \sqrt{\sigma/(\rho g)}$. This is indeed borne out in figure 5(*a*) where new dynamics emerge. In this particular configuration ($D/a \sim 2$) an air cavity is formed at the top of the drop, by its overall deformation during the impact (Bartolo, Josserand & Bonn 2006; Thoroddsen, Etoh & Takehara 2007). As this air cavity closes, it generates an internal air cylinder, and the surface deformations also generate a liquid jet which penetrates the drop to emerge at its bottom, where it punctures the film at a pronounced dimple (arrow in second frame). For this configuration the air film has not reached the critical rupture thickness, but is forced by the jet to break at the axis of symmetry, making the overall breakup dynamics essentially axisymmetric, with the edge propagating upwards towards the pool surface. These internal drop dynamics can explain the large central bubble appearing in some of the earlier studies, e.g. figure 7(*a*) in Mills *et al.* (2012).

The speed of the edge propagation can tell us something about the thickness of the air film, especially for low viscosities and thicker films, where we expect the Taylor–Culick law to hold. In figure 3(*f*) we track the tangential velocity of the edge, versus depth. It is clear that the bottom part of the air film is thickest as the hole grows much more slowly in this region, developing a thick edge of air, until it encounters a much thinner section on the sides. This sudden reduction in thickness leaves a set of large bubbles along a ring, before very fast effective motion of the breakup front ($u_e \simeq 7$ m s^{-1}; $Ca_e = 0.65$) and production of uniform bubble nets, in figure 5(*c*). Without the puncturing of the bottom jet, one would expect the film to eventually rupture at the depth where the speed is maximum.

3.6. *Larger liquid viscosities*

Figure 6(*a*) shows the contraction of the air sheet under the largest viscosity drop of silicone oil ($\nu = 1000$ cSt). The initial rupture occurs near the upper edge, often at isolated points, but the realization shown here ruptures axisymmetrically along the entire periphery and the edge moves downwards, leaving a uniform distribution of micro-bubbles. The initial velocity of the apparent edge of the film u_e, is $\sim$0.6 m s^{-1}, which is 30 times larger than the capillary–viscous velocity for this

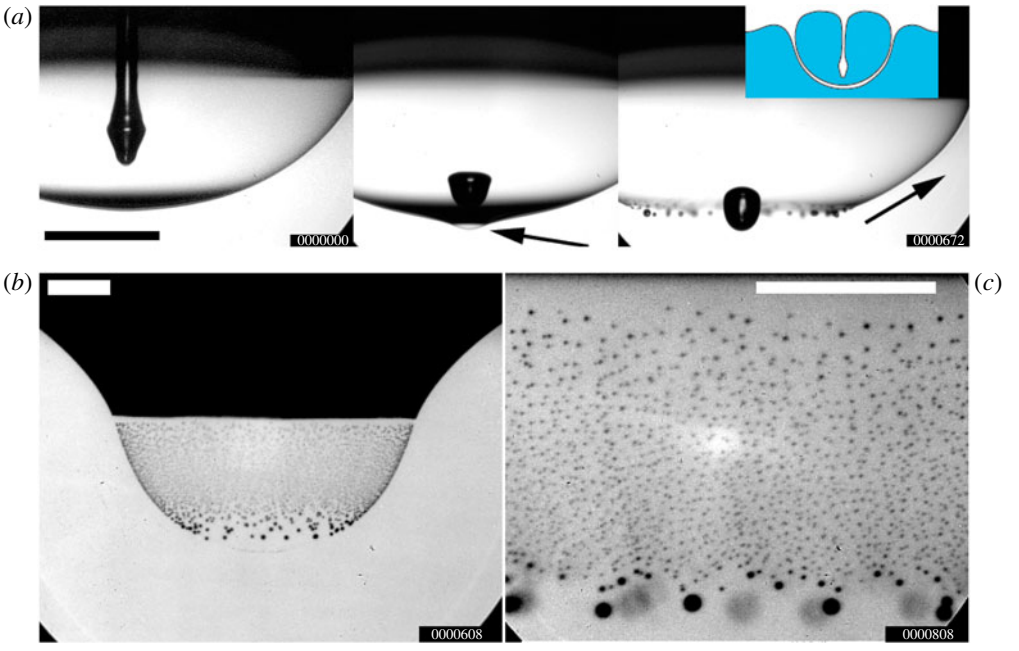

FIGURE 5. (Colour online) (*a*) Film puncturing for *perfluorohexane*, at $Re = 640$, $We = 15$. The jet generated by the collapse of the cylindrical cavity which forms at the top of the drop, penetrates to the bottom, where it pushes the air film downwards on the centreline, to form a pronounced dimple (arrow in middle frame) puncturing the film. The film subsequently retracts upwards towards the pool surface, breaking into a net of bubbles. The edge velocity is shown in figure 3(*f*). (*b*) Close-up of the bubble morphology, following punctures at the bottom tip, for silicone oil of $\nu = 1$ cSt, at $Re = 880$, $We = 16$. (*c*) Close-up of a bubble net, with a total of ∼5600 micro-bubbles produced for silicone oil of $\nu = 1$ cSt, at $Re = 980$, $We = 20$. The bars are 500 μm. See supplementary videos.

liquid, $u_\mu = \sigma/\mu \simeq 2$ cm s^{-1}. Therefore, the classical models where the film fluid is collecting in the rim cannot explain the motion of the edge. This is also illustrated in figure 6(*c*), where the horizontal edge velocity does not decrease as much as expected by the models at high viscosities. The rapid motion of the edge must therefore proceed through a different mechanism, manifest by strong edge instability and radial ruptures of the air sheet, in figure 6(*a*). In a similar way, the dewetting rates of viscous films can increase by rim instabilities (Reiter & Sharma 2001).

4. Conclusions

Herein we have imaged the various breakup mechanisms of submicron air layers caught under impacting drops. The systematic changes in the rupture depth give a clear way of estimating the *We–Oh* regime where bubble chandeliers are formed. The imaging of the resulting micro-bubbles gives us a direct estimate of the air film thickness at rupture. We have also identified a different puncture mechanism with a central jet travelling through the drop. These results will allow better estimates of the resulting air transport through air–liquid interfaces and may be the easiest way to repeatably produce such highly unstable submicron films of gas within a liquid.

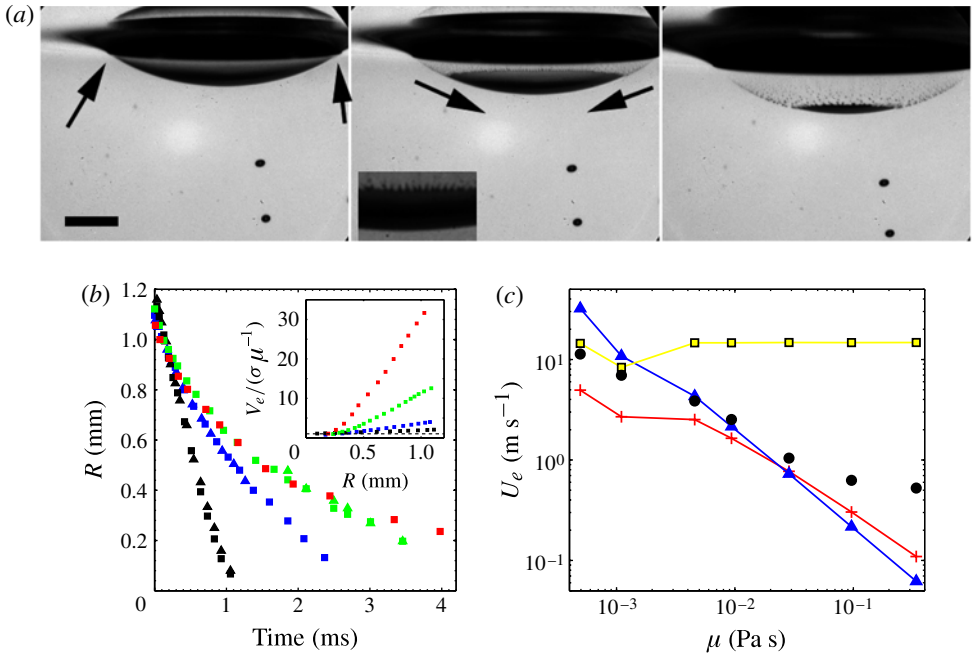

FIGURE 6. (*a*) Formation of a bubble cap for silicone oil of $\nu = 1000$ cSt, for $Re \sim 2$, $We \sim 100$, at $t = 1.15$, 1.47 and 2.69 ms after impact. Rupture starts axisymmetrically at the outer edge (arrows) in the first frame. The volume of air in the bottom bubble (3.3×10^{-4} mm^3) and all the micro-bubbles (6.9×10^{-4} mm^3, estimated by counting individual bubbles) divided by the area of the bubble cap in the first frame (3.7 mm^2) gives an average $\delta \simeq 270$ nm. The bar is 500 μm. The inset shows rupturing of the edge. (*b*) Contraction of the air cap, for $\nu = 30$ (■, ▲), 100 (▲), 350 (■, ▲), 1000 cSt (■). Inset: contraction velocity normalized by capillary viscous velocity. (*c*) Maximum horizontal edge velocity of ruptures for different viscosities (●), compared with σ/μ (▲), the logarithmic correction presented in Reyssat & Quéré (2006) (+), and Taylor–Culick velocity $\sqrt{2\sigma/(\rho\delta)}$ (□), assuming 200 nm film thickness.

Acknowledgements

S.T.T. was partly supported by KAUST–Berkeley AEA grant (cloud physics).

Supplementary videos

Supplementary videos are available at journals.cambridge.org/flm.

REFERENCES

ARYAFAR, H. & KAVEHPOUR, H. P. 2008 Hydrodynamic instabilities of viscous coalescing droplets. *Phys. Rev.* E **78** (3), 037302.

BAGUÉ, A., ZALESKI, S. & JOSSERAND, C. 2007 Droplet formation at the edge of a liquid sheet. In *6th International Conference on Multiphase Flow (ICMF2007)* (ed. M. Sommerfeld & C. Tropea). ICMF.

BARTOLO, D., JOSSERAND, C. & BONN, D. 2006 Singular jets and bubbles in drop impact. *Phys. Rev. Lett.* **96** (12), 124501.

BRENNER, M. P. & GUEYFFIER, D. 1999 On the bursting of viscous films. *Phys. Fluids* **11** (3), 737–739.

CHAN, D. Y. C., KLASEBOER, E. & MANICA, R. 2011 Film drainage and coalescence between deformable drops and bubbles. *Soft Matt.* **7** (6), 2235–2264.

COUDER, Y., FORT, E., GAUTIER, C.-H. & BOUDAOUD, A. 2005 From bouncing to floating: noncoalescence of drops on a fluid bath. *Phys. Rev. Lett.* **94** (17), 177801.

CZERSKI, H., TWARDOWSKI, M., ZHANG, X. & VAGLE, S. 2011 Resolving size distributions of bubbles with radii less than 30 μm with optical and acoustical methods. *J. Geophys. Res.* **116**, C00H11.

DEBRÉGEAS, G., MARTIN, P. & BROCHARD-WYART, F. 1995 Viscous bursting of suspended films. *Phys. Rev. Lett.* **75** (21), 3886–3889.

DHIR, V. K. 1998 Boiling heat transfer. *Annu. Rev. Fluid Mech.* **30**, 365–401.

DORBOLO, S., REYSSAT, E., VANDEWALLE, N. & QUÉRÉ, D. 2005 Aging of an antibubble. *Europhys. Lett.* **69** (6), 966–970.

ESMAILIZADEH, L. & MESLER, R. 1986 Bubble entrainment with drops. *J. Colloid Interface Sci.* **110** (2), 561–574.

ETOH, T. G., POGGEMANN, D., KREIDER, G., MUTOH, H., THEUWISSEN, A. J. P., RUCKELSHAUSEN, A., KONDO, Y., MARUNO, H., TAKUBO, K., SOYA, H., TAKEHARA, K., OKINAKA, T. & TAKANO, Y. 2003 An image sensor which captures 100 consecutive frames at 1000000 frames/s. *IEEE Trans. Electron. Devices* **50** (1), 144–151.

DE GENNES, P.-G., BROCHARD-WYART, F. & QUÉRÉ, D. 2004 *Capillarity and Wetting Phenomena: Drops, Bubbles, Pearls, Waves*. Springer.

GORDILLO, L., AGBAGLAH, G., DUCHEMIN, L. & JOSSERAND, C. 2011 Asymptotic behaviour of a retracting two-dimensional fluid sheet. *Phys. Fluids* **23** (12), 122101.

ISRAELACHVILI, J. N. 2011 *Intermolecular and Surface Forces*, third edition, pp. 253–289. Elsevier.

LHUISSIER, H. & VILLERMAUX, E. 2011 The destabilization of an initially thick liquid sheet edge. *Phys. Fluids* **23** (9), 091705.

LIOW, J.-L. & COLE, D. E. 2007 Bubble entrapment mechanisms during the impact of a water drop. In *16th Australasian Fluid Mechanics Conference, Gold Coast, Australia*, pp. 866–869. University of Queensland.

MILLS, B. H., SAYLOR, J. R. & TESTIK, F. Y. 2012 An experimental study of Mesler entrainment on a surfactant-covered interface: the effect of drop shape and Weber number. *AIChE J.* **58** (1), 46–58.

NEITZEL, G. P. & DELL'AVERSANA, P. 2002 Noncoalescence and nonwetting behaviour of liquids. *Annu. Rev. Fluid. Mech.* **34**, 267–289.

OGUZ, H. N. & PROSPERETTI, A. 1989 Surface-tension effects in the contact of liquid surfaces. *J. Fluid. Mech.* **203**, 149–171.

REITER, G. & SHARMA, A. 2001 Auto-optimization of dewetting rates by rim instabilities in slipping polymer films. *Phys. Rev. Lett.* **87** (16), 166103.

REYSSAT, É. & QUÉRÉ, D. 2006 Bursting of a fluid film in a viscous environment. *Europhys. Lett.* **76** (2), 236–242.

SAYLOR, J. R. & BOUNDS, G. D. 2012 Experimental study of the role of the Weber and capillary numbers on Mesler entrainment. *AIChE J.* doi:10.1002/aic.13764.

SIGLER, J. & MESLER, R. 1990 The behaviour of the gas film formed upon drop impact with a liquid surface. *J. Colloid Interface Sci.* **134** (2), 459–474.

SONG, M. & TRYGGVASON, G. 1999 The formation of thick borders on an initially stationary fluid sheet. *Phys. Fluids* **11** (9), 2487–2493.

THORODDSEN, S. T., ETOH, T. G. & TAKEHARA, K. 2003 Air entrapment under an impacting drop. *J. Fluid Mech.* **478**, 125–134.

THORODDSEN, S. T., ETOH, T. G. & TAKEHARA, K. 2007 Microjetting from wave focusing on oscillating drops. *Phys. Fluids* **19** (5), 052101.

VAN DER VEEN, R. C. A., TRAN, T., LOHSE, D. & SUN, C. 2012 Direct measurements of air layer profiles under impacting droplets using high-speed colour interferometry. *Phys. Rev.* E **85** (2), 026315.

WANNINKHOF, R., ASHER, W. E., HO, D. T., SWEENEY, C. & MCGILLIS, W. R. 2009 Advances in quantifying air–sea gas exchange and environmental forcing. *Ann. Rev. Mar. Sci.* **1**, 213–244.